

Article

Mechanism of Hexane Displaced by Supercritical Carbon Dioxide: Insights from Molecular Simulations

Jiasheng Song, Zhuangying Zhu and Lang Liu *

Key Laboratory of Low-Grade Energy Utilization Technologies and Systems, School of Energy and Power Engineering, Chongqing University, Ministry of Education, Chongqing 400044, China

* Correspondence: l.liu@cqu.edu.cn

Abstract: Supercritical carbon dioxide (sCO₂) has great potential for displacing shale oil as a result of its high solubility and low surface tension and viscosity, but the underlying mechanisms have remained unclear up to now. By conducting equilibrium molecular dynamics (EMD) simulations, we found that the displacing process could be divided into three steps: the CO₂ molecules were firstly injected in the central region of shale slit, then tended to adsorb on the SiO₂-OH wall surface and mix with hexane, resulting in loose hexane layer on the shale surface, and finally displaced hexane from the wall due to strong interactions between CO₂ and wall. In that process, the displacing velocity and efficiency of hexane exhibit parabolic and increased trends with pressure, respectively. To gain deep insights into this phenomenon, we further performed non-equilibrium molecular dynamics (NEMD) simulations and found that both the Onsager coefficients of CO₂ and hexane were correlated to increase with pressure, until the diffusion rate of hexane being suppressed by the highly dense distribution of CO₂ molecules at 12 MPa. The rapid transportation of CO₂ molecules in the binary components (CO₂ and hexane) actually promoted the hexane diffusion, which facilitated hexane flowing out of the nanochannel and subsequently enhanced oil recovery efficiency. The displacing process could occur effectively at pressures higher than 7.5 MPa, after which the interaction energies of the CO₂-wall were stronger than that of the hexane-wall. Taking displacing velocity and efficiency and hexane diffusion rate into consideration, the optimal injection pressure was found at 10.5 MPa in this work. This study provides detailed insights into CO₂ displacing shale oil and is in favor of deepening the understanding of shale oil exploitation and utilization.

Keywords: molecular simulations; hexane; CO₂; displacing efficiency; injection pressure



Citation: Song, J.; Zhu, Z.; Liu, L. Mechanism of Hexane Displaced by Supercritical Carbon Dioxide: Insights from Molecular Simulations. *Molecules* **2022**, *27*, 8340. <https://doi.org/10.3390/molecules27238340>

Academic Editor: Stefano Cardea

Received: 3 November 2022

Accepted: 23 November 2022

Published: 29 November 2022

Publisher's Note: MDPI stays neutral with regard to jurisdictional claims in published maps and institutional affiliations.



Copyright: © 2022 by the authors. Licensee MDPI, Basel, Switzerland. This article is an open access article distributed under the terms and conditions of the Creative Commons Attribution (CC BY) license (<https://creativecommons.org/licenses/by/4.0/>).

1. Introduction

In the past decade, the global consumption of fossil energy has tremendously increased, which increases the urgency of the development of new hydrocarbon resources [1–3]. Among the unconventional sources, shale oil has aroused extensive interest attributed to its abundant reserves, continuous distribution, and easy exploitation in comparison with the existing primary fossil energy [4–6]. Shale oil is widely presented in nano-porous shale slit through physicochemical changes such as adsorption and deposition [7–10]. Some technologies such as horizontal drilling, hydraulic fracturing, and supercritical carbon dioxide (sCO₂) displacing methods have been developed to exploit shale oil [1,11,12]. The method of sCO₂ displacing shale oil has some unique advantages, such as high solubility, swelling shale oil, low surface tension and viscosity, and enhanced crude oil recovery, compared with other technologies [13,14]. In consideration of the high efficiency involved in extracting shale oil and weakening greenhouse effects, the sCO₂ displacing shale oil technology has developed rapidly in recent years [12,15–17]. However, the underlying mechanisms of the displacing process involved have remained unclear up to now.

Some studies have compared the performance of shale oil displacing by various components, and summarized common rules in the displacing process. For instance,

Zhang et al. [18] investigated the adsorption and diffusion of shale oil in nanopores using molecular dynamics (MD) simulations. They found that the oil adsorption capacity followed the sequential order of organic matter > inorganic material > montmorillonite, and the diffusivities of octane in the shale nanopores were on the order of 10^{-9} m²/s. Zhong et al. [19] adopted four components with different polarities including decane, methyl benzene, pyridine and acetic acid in crude oil to reveal the adsorption behaviors of different sorbates on a silica surface. They found that the adsorption capability of the adsorbent was closely associated with interactions between the adsorbate and the silica surface. The polar oil components were preferentially absorbed on the mineral surface, which acted as an anchor to promote the adsorption of nonpolar counterparts.

Attributed to the essential and fundamental phenomenon, the flow and diffusion behaviors for shale gases in nano-porous shale have aroused wide attentions. By using simulations, Chen et al. [20] investigated the flow and transport of shale gas in a nano-porous shale structure. They found that shale with high tortuosity demonstrated extremely low intrinsic permeability, whereas the diffusion mode was dominated by Knudsen diffusion. In addition, the transport process was also taken into consideration by Wang et al. [21], who revealed the flow characteristics of CH₄ molecules transport through calcite nanopores, and found that the slower mass transfer arose from strong interactions and the rough inner surface.

Extensive efforts have also been devoted to the displacing process of shale oil for exploring useful methods in enhancing oil recovery. Shuai et al. [22] investigated the sCO₂ extraction process of organic matter from shale oil by experiments and simulations. They revealed that the displacement interface was more centralized as injection flow and residence increased, which could further enhance displacement rates. Lara et al. [23] studied the effect of improved oil recovery (IOR) agents, including NaCl solutions, CO₂, N₂, and CH₄ on IOR process by MD simulations. They found that CO₂ outperformed other components since its miscibility increased with pressure. Attributed to low interfacial tension and rapid diffusion in the oil phase, sCO₂ was especially suitable for IOR applications. Similar conclusions were also drawn by Nguyen et al. [24], who compared the performance of three different injection fluids, including sCO₂, N₂, and water in oil recovery, and found that sCO₂-based recovery approached 90% and outperformed the other two fluids. Seyyedi et al. [25] studied the interactions between carbonated water injection (CWI) and live crude oil through experimentation. The results revealed that CO₂ was gradually transferred to the oil, which liberated lean gases and improved oil recovery in the CW-oil system. However, the mutual mass transfer between CO₂ and oil in the CO₂-oil system led to heavier oil than the original. Lashgari et al. [15] revealed the dominant mechanisms of improved oil recovery in the injection of miscible enriched gas and CO₂. They found that the diffusion could enhance CO₂ flux delivery and contribute to oil recovery efficiency.

Apart from the essential role of the diffusion process, pressure and temperature both have an enormous influence on the displacing outcome. Fagher et al. [12] investigated oil recovery and carbon capture from shale reservoirs in the CO₂ injection process. They found that cyclic CO₂ injection had strong potential in enhancing oil recovery. The increasing pressure in conjunction with low temperature were both acted to improve oil recovery and CO₂ storage. Similar results were also obtained by Elwegaa et al. [11], who studied oil recovery from shale oil reservoirs by using cyclic cold CO₂ and found that the cold CO₂ injection enhanced both porosities and permeabilities of the core samples up to 3.5% and 8.8%, leading to a higher oil recovery factor in comparison with that at ambient temperature.

As reviewed above, the current studies mainly concentrated on adsorption and diffusion behaviors in nano-porous shale, but placed insufficient emphasis on the shale oil displacing process by sCO₂. Since the huge advantages of this technology in exploiting shale oil, the underlying mechanisms, especially the detailed displacing process, injection pressure, and mutual interference should be revealed urgently. In this study, the hydroxylated silica and hexane were adopted as shale slit and shale oil, respectively. We revealed the process of sCO₂ displacing hexane, searching for the optimal pressure by taking the

displacing velocity and efficiency, as well as the displacing mechanisms in the presence of $s\text{CO}_2$ and hexane into consideration. This study provides new insights in $s\text{CO}_2$ displacing shale oil, and supports the deepening of the understanding of shale oil exploitation and utilization.

2. Results and Discussions

2.1. CO_2 Displacing Hexane from $\text{SiO}_2\text{-OH}$ Wall

Figure 1 shows the time evolution of CO_2 displacing hexane from the $\text{SiO}_2\text{-OH}$ wall at 10.5 MPa from the initial moment, $t = 0$ ps, to $t = 200$ ps. It is seen from Figure 1 that hexane molecules adsorb stably at the wall and form a uniform oil layer at the initial moment. This distribution is gradually disturbed as CO_2 molecules diffuse into the area near the wall, occupy on the wall surface and displace hexane from the wall. As simulation time increases from $t = 20$ to $t = 40$ ps, the displacing process is clearly exhibited. More and more CO_2 molecules displace hexanes and adsorb on the wall surface. When it evolves to 100 ps, the displacing process approaches completion, and remains little difference when evolving to 200 ps. The supercritical CO_2 molecules almost completely occupy the wall surface and form several thin gas layers. As the result of CO_2 's strong dissolving capacity, the free hexanes are mixed well with CO_2 and no clusters are formed in the shale slit.

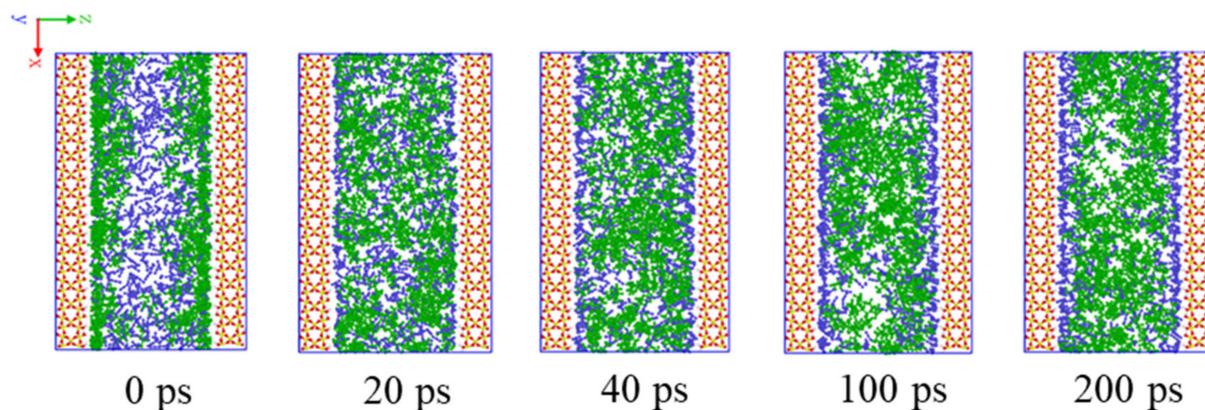


Figure 1. Snapshots of CO_2 displacing hexane from the $\text{SiO}_2\text{-OH}$ wall process from the initial moment to 200 ps in the simulation box.

To analyze the displacing process in detail, the density distributions of hexane and CO_2 along the Z direction with time were calculated and are shown in Figure 2a,b. At the initial moment ($t = 0$ ps), the density of hexane exhibits two symmetrical peaks about 0.73 g/cm^3 near the wall. The two-layer hexanes adsorb firmly on the wall surface, and form two stable oil layers. However, the hexane density decreases to nearly 0.05 g/cm^3 at the center location. This huge distribution difference gradually diminishes as simulation time reaches 100 ps. At this time, the hexane molecules distribute uniformly in the bulk region, while the density gradually decreases to near zero when approaching the wall. This can be understood that hexane molecules are displaced by CO_2 thoroughly from the wall, while the density of CO_2 approaches to the maximum. It can be seen from Figure 2b that the evolution of CO_2 density distribution with time is opposite to that of hexane. The density variation trends of CO_2 and hexane have explicitly elucidated the procedure of CO_2 displacing hexane adsorbed on the shale wall, which is the same as the snapshots shown in Figure 2.

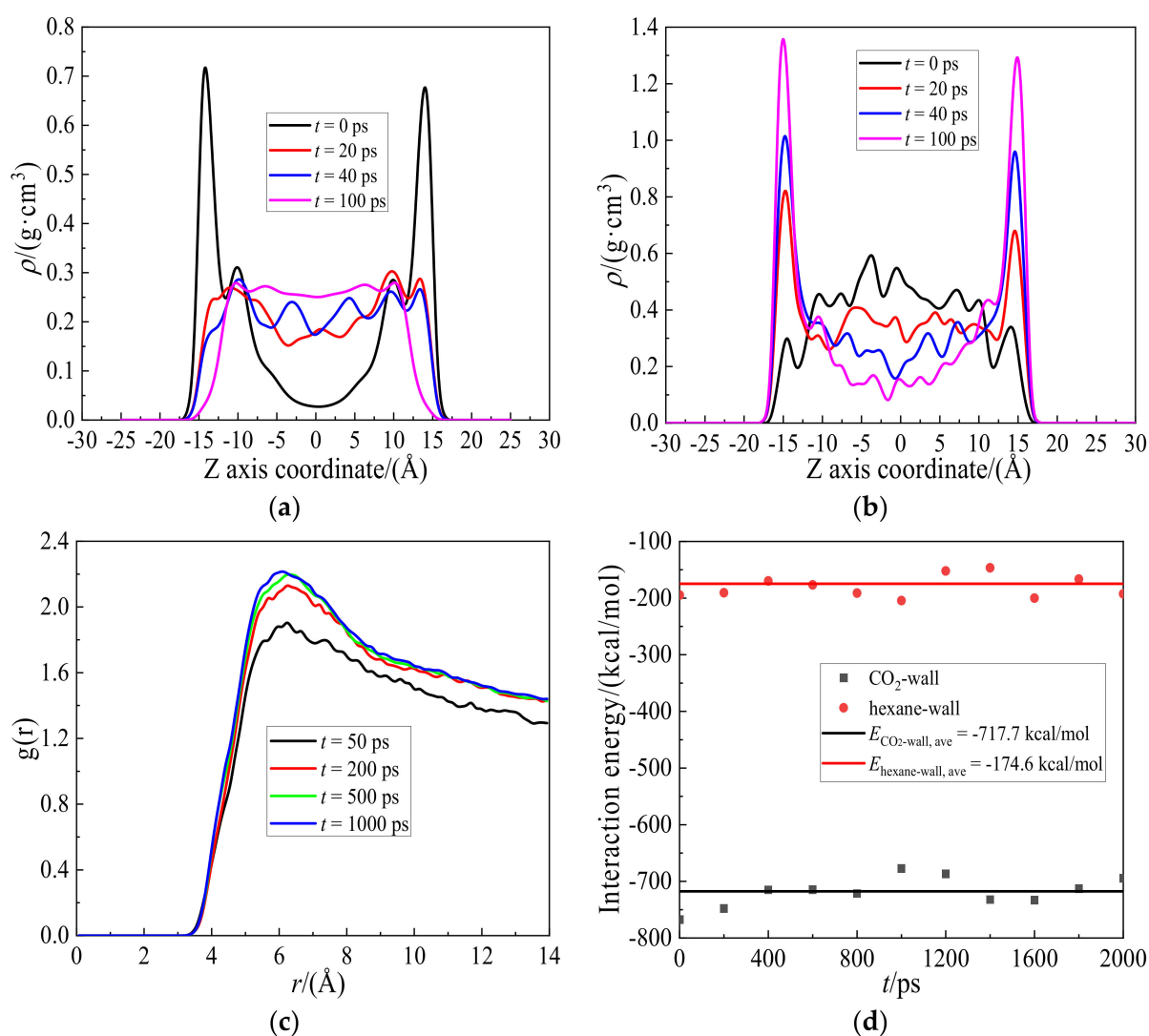


Figure 2. Density distributions of (a) hexane and (b) CO₂ along the Z axis direction from the initial moment to 100 ps. (c) Radial distribution functions, $g(r)$, of carbon-to-carbon atoms in CO₂, C-C, from 50 to 1000 ps. (d) Variations of interaction energies of hexane-wall and CO₂-wall with time from initial moment to 2000 ps.

Figure 2c shows radial distribution functions, $g(r)$, of carbon-to-carbon atoms, C-C, in CO₂ molecules from 50 to 1000 ps. It can be seen from Figure 2c that the peak values of $g(r)$ decrease with time, indicating that the distribution for CO₂ at 6.2 Å becomes less tight as time evolves. As the displacing process continues, CO₂ molecules distribute widely in the whole system, resulting in fewer CO₂ molecules around each other. Due to strong interactions between the CO₂ and SiO₂-OH wall, some CO₂ molecules adsorb and gradually aggregate on the wall surface, resulting in slightly denser distribution. In this study, the interaction energy between CO₂ and the wall drives hexane away from the wall.

Figure 2d shows the variations of interaction energies for the hexane-wall and the CO₂-wall with time from the initial moment to 2000 ps. The interaction energies of the hexane-wall and CO₂-wall, $E_{\text{hexane-wall}}$ and $E_{\text{CO}_2\text{-wall}}$, are stabilized at -174.6 and -717.7 kcal/mol respectively and kept almost constant in the simulation process. The stronger interactions of the CO₂-wall in comparison with the hexane-wall's render CO₂ preferentially occupy hexane's locations on the wall surface and displace hexane from it. Plenty of hexanes are driven to fall into the shale slit and mix with CO₂ molecules. Therefore, the whole displacing process is completed.

2.2. Effect of CO₂ Injection Pressure on Hexane Displacement

Figure 3 shows variations of snapshots of CO₂ displacing hexane from the SiO₂-OH wall at the equilibrium state with injection pressures from 6.0 to 12.0 MPa. As shown in Figure 3, the amount of CO₂ adsorbed on the wall increases with pressures from 6.0 to 9.0 MPa, and keeps almost constant at pressures higher than 9.0 MPa. The increasing and then nearly constant trends show unsaturated and saturated adsorption states for CO₂ on the wall, resulting in the increasing and constant thickness of the adsorption layer respectively. The limited adsorption capacity of the SiO₂-OH wall cannot hold more CO₂ molecules after saturated adsorption, allowing some desorbed ones to diffuse in the shale slit, thereby destroying the cluster structure that may have formed previously.

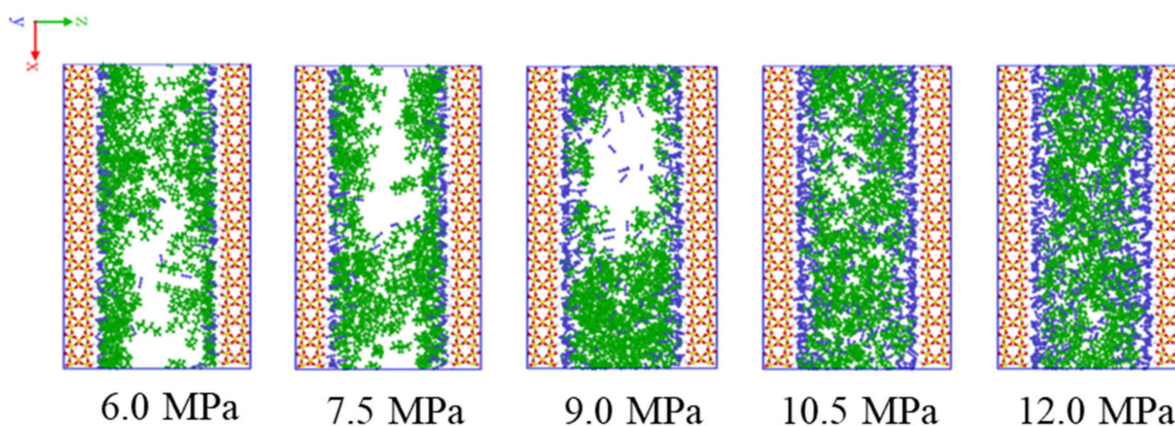


Figure 3. Variations of snapshots of CO₂ displacing hexane from the SiO₂-OH wall at the equilibrium state with injection pressures from 6.0 to 12.0 MPa.

Figure 4 shows the density distributions of hexane and CO₂ along the Z axis direction at pressures from 6.0 to 12.0 MPa. The density of hexane near the wall and in the shale slit gradually decreases and increases as pressure increases from 6.0 to 12.0 MPa, respectively. The uniform density distribution along Z direction of hexane is opposite to CO₂'s at higher pressure in Figure 4b, as revealed in the previous section. At low pressure, there are still some hexanes remaining on the unsaturated wall surface. As pressure increases, more CO₂ molecules adsorb on the wall and displace the rest of the hexanes from the wall. The hexanes are pushed into the shale slit, while the CO₂ molecules are aggregated on the wall. Therefore, the densities of hexanes and CO₂ molecules exhibit opposite trends, in agreement with the snapshots in Figure 3.

To quantitatively analyze the displacement performance, Figure 5 illustrates the time evolution of the number of hexanes being displaced from the wall by CO₂ injections with different pressures. It can be seen from Figure 5a that the number of hexanes departing from the wall, n , increases linearly with time, t , and remains almost constant after a certain time frame. By linearly fitting the displacing number, n , with time t , $n \sim t$, in the linear area the displacing velocity, v , was obtained and shown in Figure 5b. The displacing velocity increases from 0.96 to 1.51 ps⁻¹, when CO₂ injection pressure increases from 6.0 to 10.5 MPa, and then decreases to 1.33 ps⁻¹ at 12.0 MPa. As pressure increases from 6.0 to 10.5 MPa, CO₂ molecules displace hexane from the wall more rapidly due to enhanced adsorption. However, the hindrance effect is enhanced as pressure increases to 12.0 MPa. Some unabsorbed CO₂ molecules in the shale slit can be a hindrance to hexane diffusion, which could slow down the displacing velocity of hexane. Therefore, the optimal pressure in the displacing velocity is 10.5 MPa.

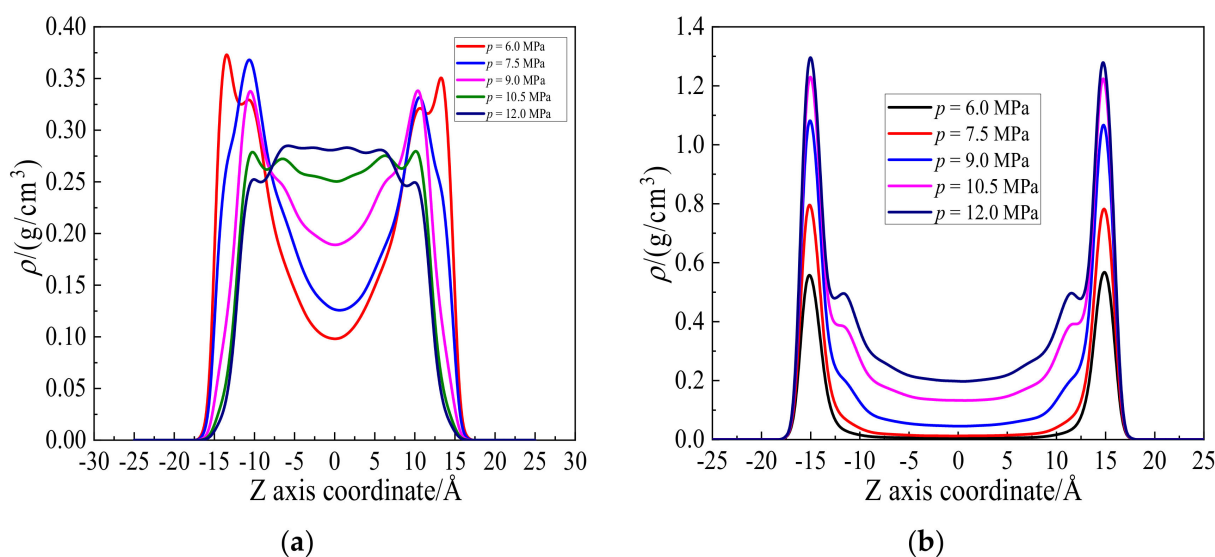


Figure 4. Density distributions of (a) hexane and (b) CO₂ along Z axis direction at pressures from 6.0 to 12.0 MPa.

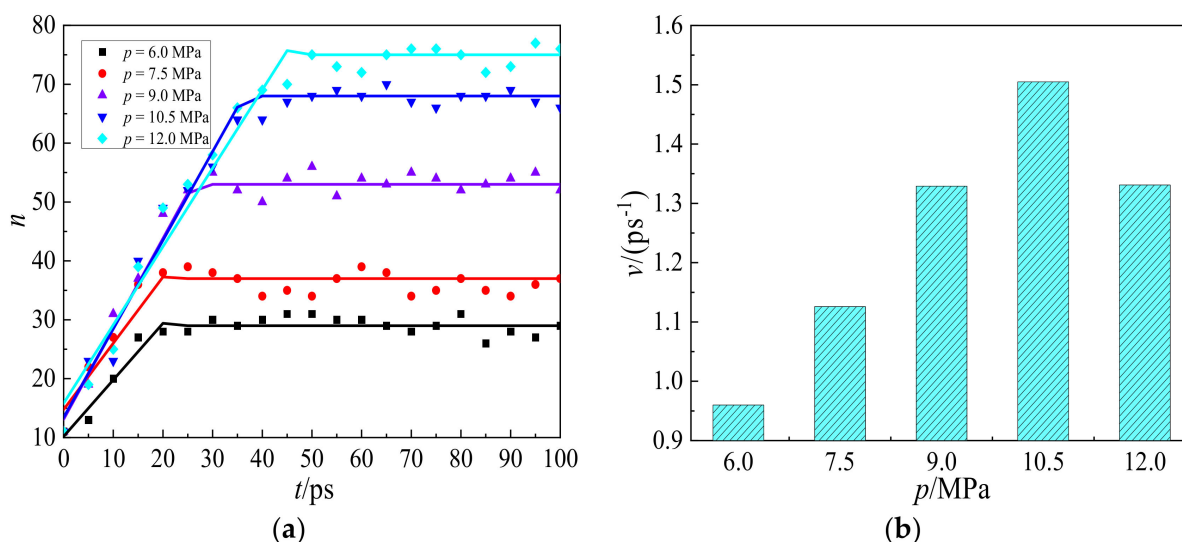


Figure 5. (a) Variations of the number of hexanes, n , displacing from the wall with time, t , from the initial moment to 100 ps, and (b) the displacing velocity of hexanes, v , at pressures from 6.0 to 12.0 MPa. The displacing velocity was obtained from the linear area in Figure 5a.

The displacing velocity, v , cannot directly tell the recovering efficiency under the practical conditions, which is essential to unconventional shale oil production industry. To address this problem, the displacing efficiency, η , is accordingly proposed and defined as,

$$\eta = \frac{n}{N} \quad (1)$$

where, n and N represent the number of hexanes displacing from the wall and the total number of hexanes in the system, respectively. According to Figure 5a, the number of hexanes displacing from the wall, n , keeps almost constant at equilibrium after 50 ps. In that case, the number, n , was counted and averaged. As shown in Figure 6, the displacing efficiency of hexane, η , increases from 16.3% to 42.1%, when the injection pressure increases from 6.0 to 12.0 MPa. At lower pressure, the adsorption of CO₂ in the shale slit pore is still far away from saturation. As the pressure increases further, additional CO₂ molecules adsorb on the wall surface and displace the hexane from the wall surface for the enhanced

adsorption affinity of CO₂. Nevertheless, such an increasing trend of displacing efficiency slows down at higher pressure due to the steric hindrance effect in the shale slit. As shown in Figures 3 and 4b, the shale slit is full of CO₂ and hexane molecules, rendering it more difficult to further conduct the displacing process. Taking both displacing velocity and efficiency into consideration, the optimal injection pressure is 10.5 MPa.

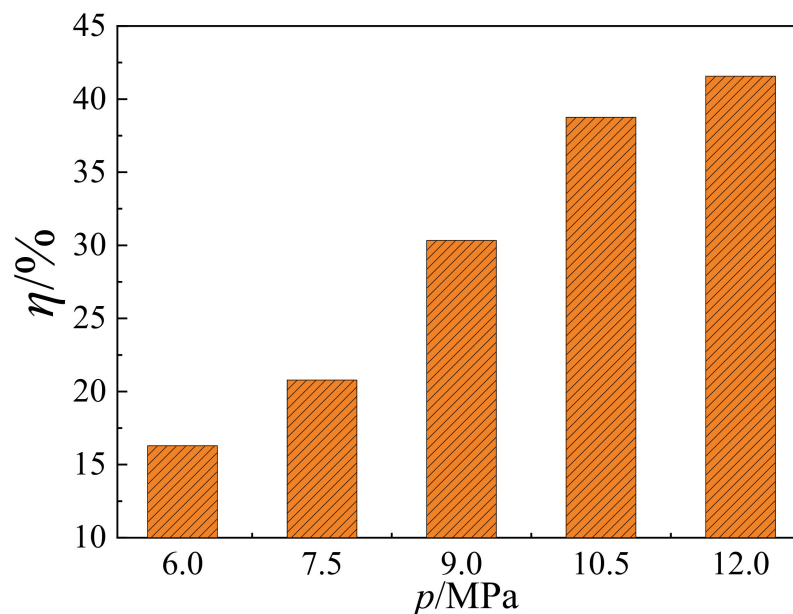


Figure 6. Variations of displacing efficiency for hexane, η , with pressures from 6.0 to 12.0 MPa.

2.3. Mechanisms of CO₂ Injection Pressure on the Hexane Displacing Process

To reveal the underlying mechanisms of the displacing process, NEMD simulations were further conducted to analyze the binary mixture diffusion. The force, Γ_{ex} , exerting on the molecules to drive the fluid flow can be expressed as,

$$\Gamma_{ex} = -\frac{d\mu}{dz} = -k_B T \frac{d \ln f}{dz} = k_B T \frac{\ln(f_1/f_2)}{L_x} \quad (2)$$

where, k_B , T , f_1 , f_2 , and L_x are Boltzmann constant, temperature, inlet fugacity, outlet fugacity, and length of the simulation box, respectively. According to the relationship between the external force and net flux, the Onsager coefficient, L_{ij} , can be obtained and expressed as,

$$\begin{bmatrix} j_1 \\ j_2 \end{bmatrix} = - \begin{bmatrix} L_{11} & L_{12} \\ L_{21} & L_{22} \end{bmatrix} \begin{bmatrix} \frac{\partial \mu_1}{\partial z} \\ \frac{\partial \mu_2}{\partial z} \end{bmatrix} = \begin{bmatrix} L_{11} & L_{12} \\ L_{21} & L_{22} \end{bmatrix} \begin{bmatrix} \Gamma_{ex1} \\ \Gamma_{ex2} \end{bmatrix} \quad (3)$$

here, j_i , L_{ii} , and L_{ij} are net flux of component i , Onsager coefficients of diagonal and off diagonal respectively. The net flux, j , can also be computed by equation, $j_i = \rho_i \cdot v_{com,i}$. Here, ρ_i and $v_{com,i}$ are density and streaming velocity of component i , respectively. Γ_{ex} is the external force exerting on the component i , and expressed as, $\Gamma_{ex,i} = -\partial \mu_i / \partial z$. The hexane and CO₂ are marked as components 1 and 2 respectively in this study. We note that by only applying external force to single component i (i.e., $\Gamma_{ex,i} > 0$, $\Gamma_{ex,j} = 0$), the net fluxes can be obtained according to equation, $j_i = \rho_i \cdot v_{com,i}$. Accordingly, the Onsager coefficients L_{11} and L_{22} for hexane and CO₂, can be extracted by $L_{11} = j_1 / \Gamma_{ex1}$ and $L_{22} = j_2 / \Gamma_{ex2}$, respectively. Meanwhile, the diagonal Onsager coefficients L_{12} and L_{21} are calculated as, $L_{12} = j_1 / \Gamma_{ex2}$ and $L_{21} = j_2 / \Gamma_{ex1}$, respectively.

As depicted in Figure 7a,b, the driven streaming velocities of hexane and CO₂ exhibit good linear relationships with external forces. This further reveals that the diagonal Onsager coefficients are independent with external force. Figure 7c shows variations of diagonal Onsager coefficients with pressures from 6.0 to 12.0 MPa. It can be seen from

Figure 7c that the diagonal Onsager coefficients, L_{12} and L_{21} , exhibit good agreements with each other, and satisfy well with Onsager reciprocal relation. It can be inferred from this result that the mutual diffusion plays an essential role in the displacing process and will be revealed in detail in the following parts.

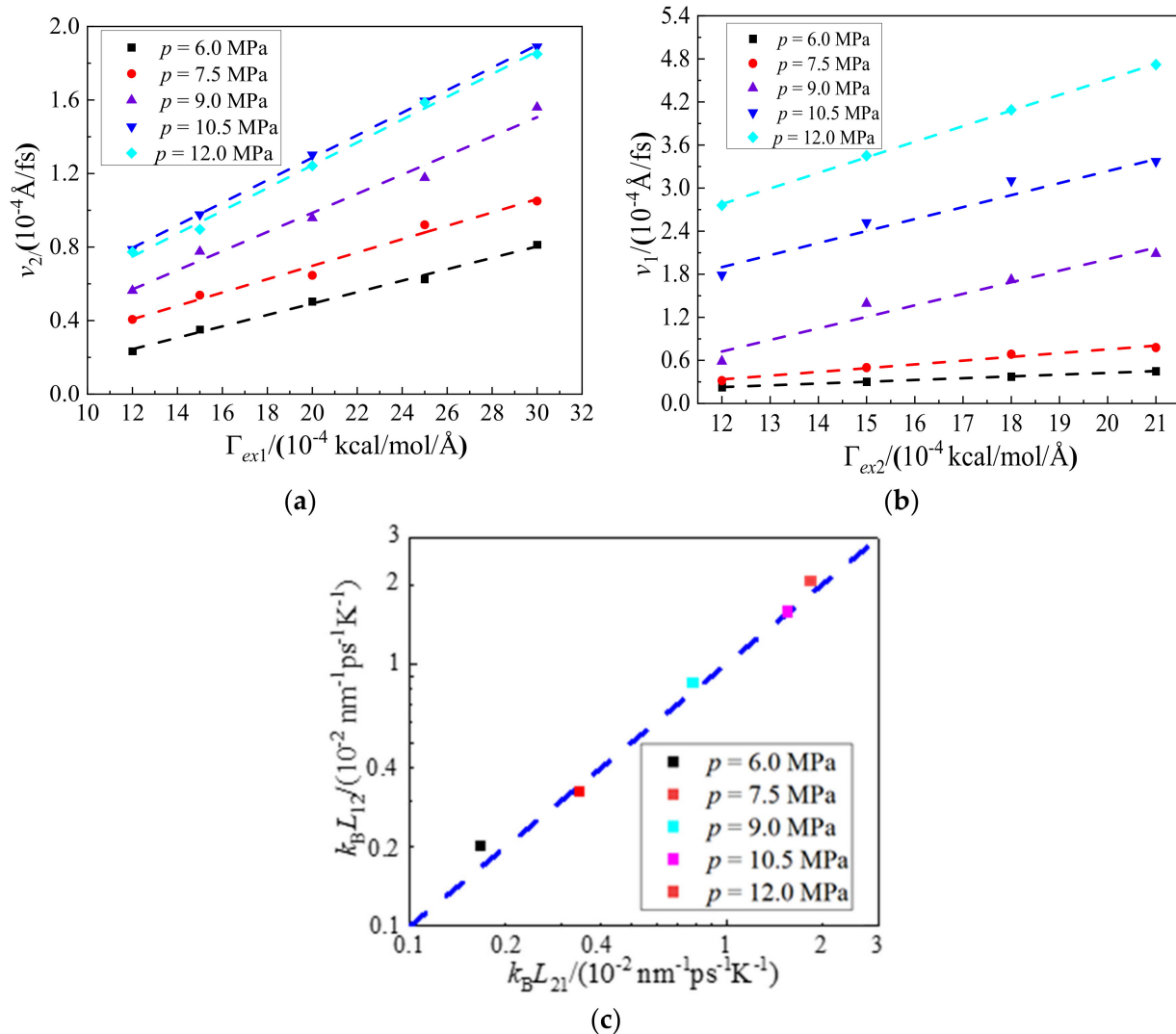


Figure 7. Variations of (a) CO₂ velocity, v_2 , when external forces, Γ_{ex1} , are applied on hexane, (b) hexane velocity, v_1 , when the other external forces, Γ_{ex2} , are applied on CO₂, and (c) diagonal Onsager coefficients L_{12} and L_{21} , with injection pressures from 6.0 to 12.0 MPa. The blue dotted line, $y = x$, represents the isoline of the horizontal and vertical axes, $L_{12} = L_{21}$.

The velocities, v , and Onsager coefficients, L_{ij} , for hexane and CO₂, at pressures from 6.0 to 12.0 MPa are shown in Figure 8. It can be seen from Figure 8a that the velocity of hexane increases linearly with force. We can further see that the Onsager coefficients of hexane increase from 0.325×10^{-2} to $0.481 \times 10^{-2} \text{ nm}^{-1} \text{ ps}^{-1} \text{ K}^{-1}$, when the pressure of CO₂ increases from 6.0 to 10.5 MPa. Nevertheless, the Onsager coefficient of hexane decreases after that and slightly reduces to $0.465 \times 10^{-2} \text{ nm}^{-1} \text{ ps}^{-1} \text{ K}^{-1}$ at the pressure of CO₂ being 12.0 MPa. It should be pointed out that the injected sCO₂ not only displaces the oil from the shale wall, evident from Figure 8, but also generally enhances the diffusion rate of oil (hexane). That is to say, the presence of sCO₂ will render it easier for oil to leave out the shale channel. In combining these two effects, one can expect that the sCO₂ displacing oil method will achieve high recovery efficiency while reducing the oil exploiting time.

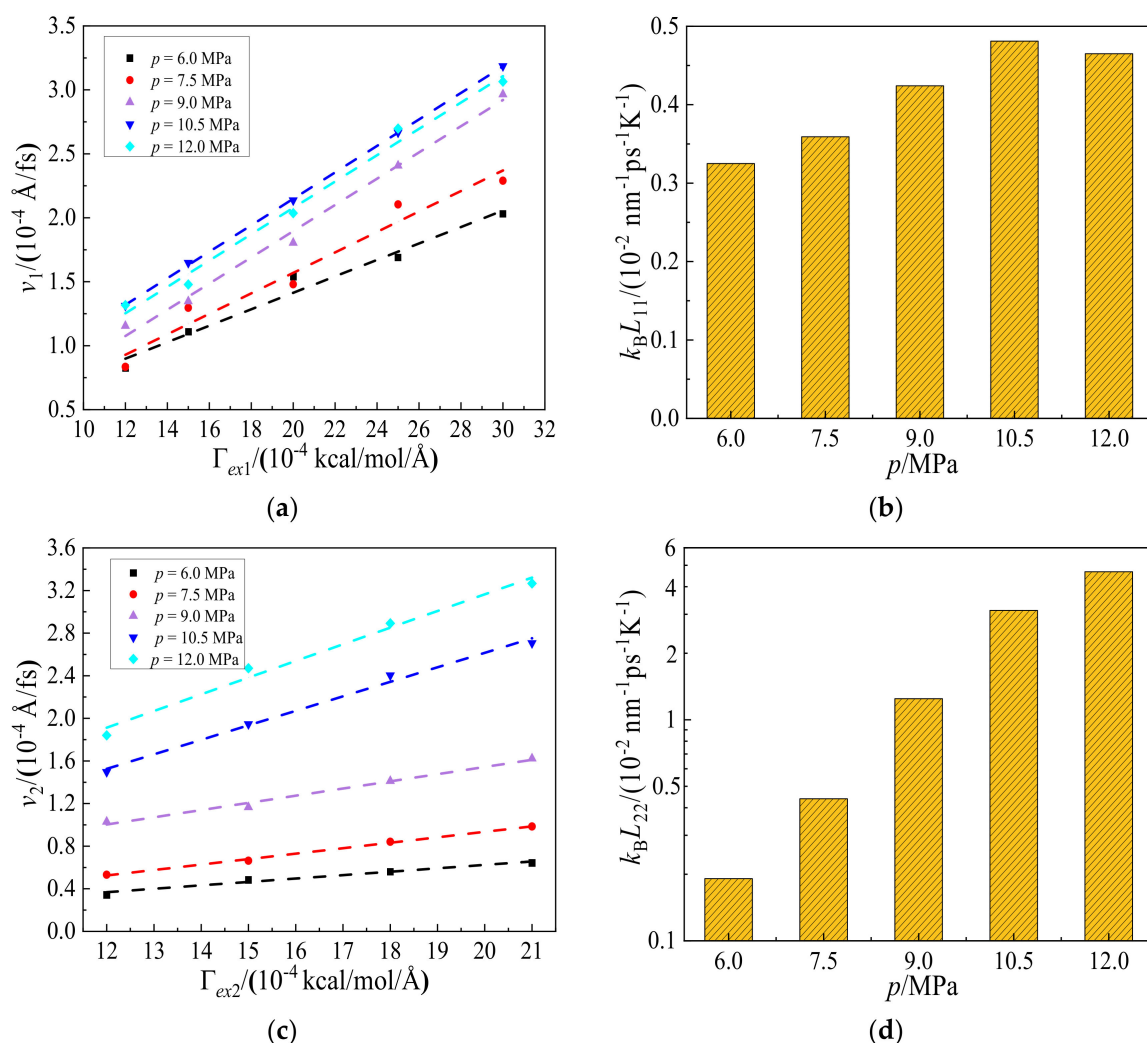


Figure 8. Variations of (a) velocity, v_1 , and (b) Onsager coefficient, $k_B L_{11}$, of hexane when external forces, Γ_{ex1} , are applied on hexane, (c) velocity, v_2 , and (d) Onsager coefficient, $k_B L_{22}$, of CO₂ when the other external forces, Γ_{ex2} , are applied on CO₂, at pressures from 6.0 to 12.0 MPa with 1.5 MPa internals, respectively.

Meanwhile, it can be seen from Figure 8d that the Onsager coefficient of CO₂ increases rapidly with pressure. At lower pressures (6.0 and 7.0 MPa), CO₂ molecules diffuse slowly due to a larger number of them adsorbing on the wall surface. With increasing pressure to 9.0 and 10.5 MPa, the diffusion of CO₂ molecules accelerates sharply. At 12.0 MPa, the Onsager coefficient of CO₂ is $4.68 \text{ nm}^{-1} \text{ps}^{-1} \text{K}^{-1}$, which is over an order of magnitude higher than that of hexane, $0.465 \text{ nm}^{-1} \text{ps}^{-1} \text{K}^{-1}$. However, the highest pressure corresponding to the highest diffusion for CO₂ molecules reduces hexane diffusion, which can reduce shale oil recovery efficiency. In consideration of the displacing velocity, the optimal injection pressure is 10.5 MPa.

Figure 9 shows the interaction energies of the hexane-wall and CO₂-wall with pressures from 6.0 to 12.0 MPa. It can be seen from Figure 9 that the interaction energies for the hexane-wall and the CO₂-wall decrease and increase with pressure in the range studied. For instance, the interaction energies for the CO₂-wall increase from -478.8 to -737.6 kcal/mol, while that for the hexane-wall decrease from -575.3 to -134.2 kcal/mol, when the pressure increases from 6.0 to 12.0 MPa. At higher pressure, CO₂ molecules distribute more densely near the wall, leading to stronger CO₂-wall interaction energies, which is similar to the results given in previous studies [26,27]. The dominant interaction energies shift from hexane-wall to CO₂-wall at 7.5 MPa, which shows that CO₂ molecules are more inclined to

adsorb on the wall surface and displace hexane from the surface. It can be understood that the further distance between the hexane and the wall weakens the interactions between them according to Equation (2). On the other hand, the stronger CO₂-wall interactions drive more hexane molecules away from the wall, resulting in most hexane distributing in the bulk region, which is in agreement with the results in the previous part.

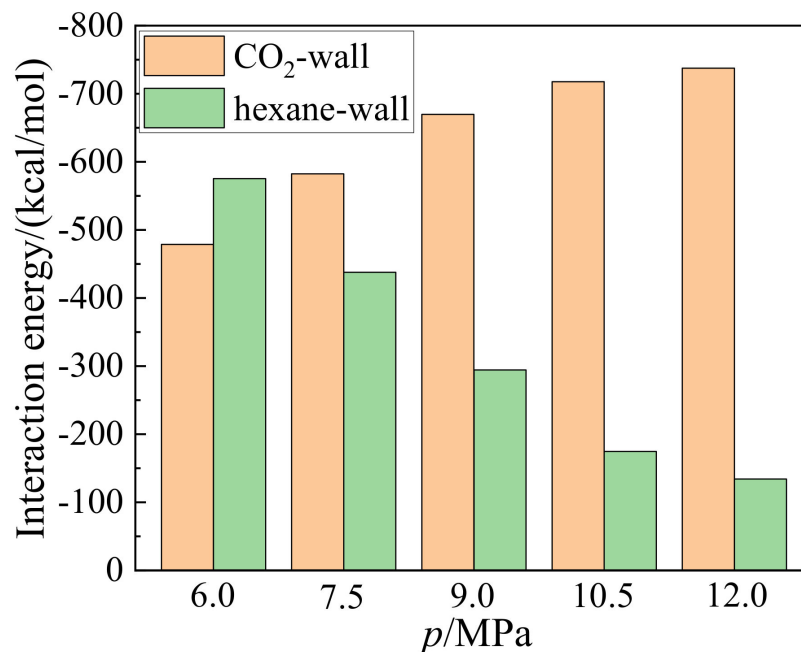


Figure 9. Variations of interaction energies of hexane-wall and CO₂-wall with pressures from 6.0 to 12.0 MPa with 1.5 MPa internals.

3. Materials and Methods

3.1. Model and Configurations

The simulation setup is comprised of three sections, including two hydroxylated silica crystal (SiO₂-OH) walls located at the upper and lower edges of the box, creating a channel with the flowing direction being the x axis, as shown in Figure 10b. The chemical structure of the shale wall, SiO₂-OH, is illustrated in Figure 10a. The dimensions of the simulation box, $L_x \times L_y \times L_z$, are set as $78.56 \times 48.62 \times 50 \text{ \AA}^3$. There are full of chain alkane such as hexane, n-decane, and tetradecane in nano scale shale. Among these alkanes, hexane accounts for a large percentage and has many typical properties. In addition, hexane can well reflect the performances of shale oil in the nanochannel and can work as a representative in extensive studies [18,23,28]. Therefore, hexane was the adopted and represented oil in this study. A snapshot of the integrated simulation system is depicted in Figure 10b.

The simulations were performed as follows. Firstly, the process of CO₂ displacing hexane was conducted. In that case, the movement and density distribution of CO₂ and hexane were discussed. Secondly, the effects of injection pressures of CO₂, which range from 6.0 to 12.0 MPa with 1.5 MPa intervals, on the displacing process were investigated to figure out the optimal pressure, evaluated by displacing velocity and efficiency. Finally, the corresponding underlying mechanisms of the displacing process were further explored.

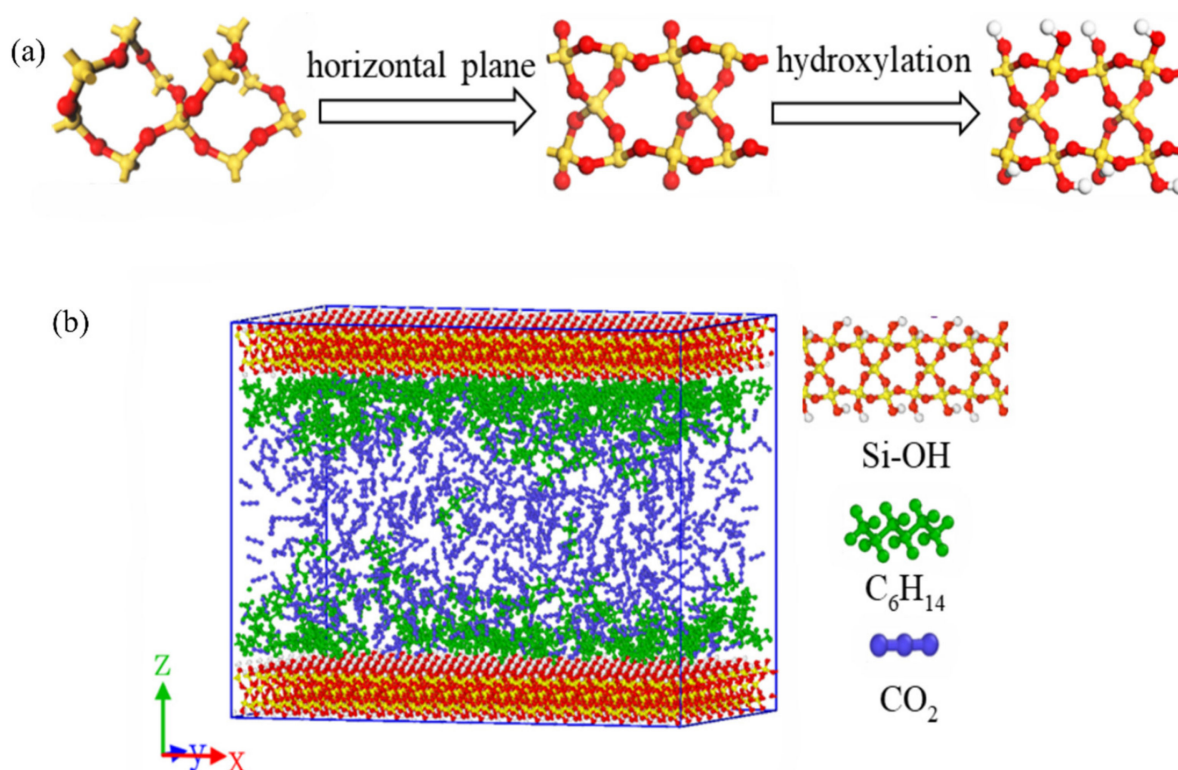


Figure 10. (a) Hydroxylation process of silica, $\text{SiO}_2\text{-OH}$, and (b) Simulation setup. The walls at the upper and lower edges are hydroxylated silica, $\text{SiO}_2\text{-OH}$, in which the red, yellow, and white spheres represent oxygen, silica, and hydrogen atoms, respectively. The green and blue molecules in the shale slit are hexane (C_6H_{14}) and carbon dioxide (CO_2) respectively.

3.2. Force Fields of Adsorbent and Adsorbates

Adsorbate-adsorbate, adsorbent-adsorbate interactions were both explicitly considered in our simulations. Initially, hexane molecules were described by OPLS-AA force fields [29], which are comprised of bond contraction energy, E_{bonds} , angular bending energy, E_{angle} , dihedral angle torsion energy, $E_{torsions}$, van der Waals interaction energy, E_{vdW} , and electrostatic interaction energy, E_{ele} , expressed as,

$$E_{all} = E_{bonds} + E_{angles} + E_{torsions} + E_{vdW} + E_{ele} \quad (4)$$

The detailed parameters of the OPLS-AA model for hexane are shown in Tables 1–4. The flexible CO_2 molecule was represented by the EPM2 model [30], with detailed parameters being listed in Tables 1, 2 and 4. In addition, CLAYFF force fields were adopted to describe the $\text{SiO}_2\text{-OH}$ wall [31] given in Tables 1, 2 and 4. The force fields of species, including hexane, CO_2 and $\text{SiO}_2\text{-OH}$, adopted in this work have been verified to be effective in adsorption and diffusion in extensive studies [18,19,32].

Table 1. Bond parameters of C_6H_{14} , CO_2 and $\text{SiO}_2\text{-OH}$ adopted here.

Species	Bond Type	K_r (kcal/mol)	r_0 (Å)
C_6H_{14}	C-C	268.0	1.529
	C-H	340.0	1.09
CO_2	C=O	615.322	1.149
$\text{SiO}_2\text{-OH}$	O-H	554.1349	1.0

Table 2. Angle parameters of C₆H₁₄, CO₂ and SiO₂-OH.

Species	Angle Type	K _θ (kcal/(mol·rad ²))	θ (°)
C ₆ H ₁₄	C-C-C	58.35	112.70
	C-C-H	37.5	110.70
	H-C-H	33.0	107.80
CO ₂	O=C=O	295.411	180
SiO ₂ -OH	Si-O-H	30.0	109.47

Table 3. Dihedral angle parameters of OPLS-AA model for C₆H₁₄.

Types	V ₁ (kcal/mol)	V ₂ (kcal/mol)	V ₃ (kcal/mol)	V ₄ (kcal/mol)
C-C-C-C	1.30	−0.05	0.30	0
C-C-C-H	0	0	0.30	0
H-C-C-H	0	0	0.30	0

Table 4. Lennard-Jones 12–6 potentials and charges of atoms.

Species	Atoms	ε (kcal/mol)	σ (Å)	q (e)
SiO ₂ -OH	Si	1.84 × 10 ^{−6}	3.302	+2.1
	O	0.1554	3.1655	−1.05
	O_OH	0.1554	3.1655	−0.95
	H_OH	0	0	0.425
C ₆ H ₁₄	C_CH ₃	0.066	3.50	−0.18
	C_CH ₂	0.066	3.50	−0.12
	H_C ₆ H ₁₄	0.030	2.50	0.06
CO ₂	C_CO ₂	0.0559	2.757	0.6512
	O_CO ₂	0.1559	3.033	−0.3256

In addition to the bonded interactions, the nonbonded ones, including short-range (Lennard-Jones 12–6) and long-range force fields are also summed to describe interactions among atoms, expressed as,

$$U = 4\epsilon \left[\left(\frac{\sigma}{r_{ij}} \right)^{12} - \left(\frac{\sigma}{r_{ij}} \right)^6 \right] + \frac{q_i q_j}{4\pi\epsilon_0 r_{ij}} \quad (5)$$

herein, ϵ and σ are potential well depth and collision distance, respectively. The LJ parameters between two unlike species were calculated from the Lorentz-Berthelot mixing laws [33], following

$$\epsilon_{ij} = \sqrt{\epsilon_i \epsilon_j} \quad (6)$$

$$\sigma_{ij} = \frac{\sigma_i + \sigma_j}{2} \quad (7)$$

3.3. Simulation Configurations

The equilibrium and nonequilibrium molecular dynamics (EMD and NEMD) simulations were conducted using LAMMPS packages [34], starting with the initial configurations obtained from grand canonical Monte Carlo (GCMC) simulations that were conducted at 353.15 K throughout the simulations and targeted pressure using DL_MONTE simulation packages [35]. The NEMD simulations were performed by exerting external force on one of the two components in the presence of the sCO₂ and hexane mixtures. The Nosé-Hoover thermostat was applied to maintain the temperature of the system with a damp coefficient of 100 fs. In all simulations, the cutoff radius equaling 14.0 Å was applied to truncate short-range and long-range interactions in the real space. The Ewald method with a tolerance of 1.0 × 10^{−4} was adopted for the long-range corrections to the coulomb interactions. The time step was set as 1.0 fs and periodic boundary conditions were applied in all three

directions. The simulations were performed for 4.0 ns in the canonical ensemble with the first 2.0 ns for equilibration and the remaining 2.0 ns for statistical analysis at a frequency of 500 steps. The temperature of the system remains at 353.15 K as it is the critical temperature of sCO₂. We computed the density and number of CO₂ molecules in the simulation system using grand canonical Monte Carlo simulations (GCMC) at different pressures, which are listed in Table 5. In our simulations, the number of hexane molecules is 178. Indeed, the number of hexanes remains constant in this work. This is done for the two reasons: (1) In practice, the sCO₂ molecules are injected into the shale oil reservoir, with the temperature and pressure of the shale oil reservoir being fixed, which leads to a fixed content of oil molecules for a given reservoir. Therefore, it is justified to investigate the efficiency of sCO₂ dispatching the oil by fixed the molecule numbers adsorbed on the shale wall. (2) The second reason is for controlling the variable without neglecting the essential performance. Although the hexane density can be varied at different pressures (i.e., different depths of the reservoirs), the displacing process is basically unchanged. To elucidate the process and its underlying mechanisms more clearly, some necessary simplifications were conducted in this work. This treatment can not only reveal the main mechanisms and characteristics, but also save computation costs. Therefore, the number of hexane molecules remains constant in this work.

Table 5. Variations of density and number of CO₂ molecules at 353.15 K with pressures.

p (MPa)	ρ (g·cm ⁻³)	Number
6.0	0.14688	246
7.5	0.22847	394
9.0	0.3745	637
10.5	0.5551	961
12.0	0.6728	1173

3.4. Verification of the Simulation

To confirm the accuracy and reliability of this work, the potentials were verified. The density and self-diffusion coefficient for CO₂ represented by the EMP2 model at different temperatures and pressures were calculated and shown in Figure 11a,b, respectively. It can be seen from Figure 11a,b that the CO₂ density and self-coefficient are close to the results in the database of the American National Standards Institute. Indeed, the standard error between the two is within 6.0%, matching well with each other. As shown in Figure 11b, the self-diffusion coefficients of CO₂ decrease/increase with pressure/temperature in a wide range, which caters well to the trend reported in previous studies [36,37].

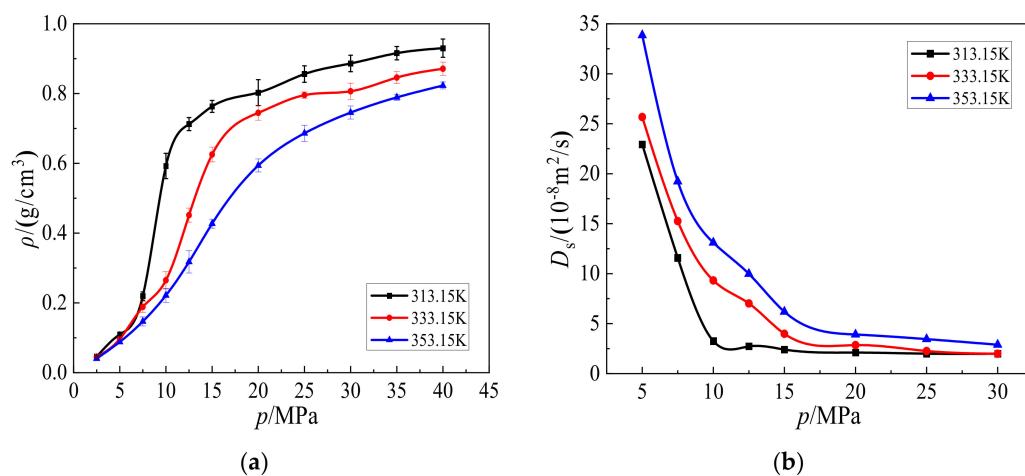


Figure 11. Variations of (a) density and (b) self-diffusion coefficient for CO₂ at different temperatures and pressures from 6.0 to 12.0 MPa.

4. Conclusions

Molecular dynamics simulations were performed to explore process of CO₂ displacing hexane from SiO₂-OH wall, the effects of CO₂ pressure on the displacing velocity and efficiency as well as the underlying oil recovering mechanisms in binary mixtures are discussed in detail. The displacing process can be divided into three steps; first, supercritical CO₂ molecules fill in the shale slit, and then adsorb on the wall surface and mix with hexane, resulting in a loose hexane layer, and they finally displace the hexane from the wall due to stronger interactions between CO₂ and the wall. The displacing velocity increases to a maximum at 10.5 MPa, and then decreases with pressure. In addition, the displacing efficiency increases from 16.3% to 42.1% when pressure increases from 6.0 to 12.0 MPa. This phenomenon is caused by the change in diffusion circumstance, in which the Onsager coefficients of CO₂ and hexane are correlated to increase with pressure, until the diffusion rate of hexane being suppressed by the highly dense distribution of CO₂ molecules is equal to 12 MPa. Indeed, the rapid transportation of CO₂ molecules in the binary components (CO₂ and hexane) promotes the hexane diffusion, which is in favor of driving oil out of nanochannels. The interaction energies of the CO₂ wall are stronger than that of the hexane wall when pressures are higher than 7.5 MPa, which originally accounts for the efficient hexane displacement. Taking the displacing velocity and efficiency and the hexane diffusion rate into consideration, the optimal injection pressure of CO₂ is 10.5 MPa in this work. Our study provides detailed mechanisms of CO₂ displacing hexane from a wall, which contributes to a deeper understanding of unconventional oil and gas exploitation and utilization.

Author Contributions: Conceptualization, Z.Z. and L.L.; methodology, L.L.; software, Z.Z.; validation, J.S., Z.Z. and L.L.; formal analysis, Z.Z.; investigation, Z.Z.; resources, L.L.; data curation, J.S.; writing—original draft preparation, J.S.; writing—review and editing, J.S. and L.L.; visualization, Z.Z.; supervision, L.L.; project administration, L.L.; funding acquisition, L.L. All authors have read and agreed to the published version of the manuscript.

Funding: This research was funded by National Natural Science Foundation of China [Grant No. 52006017] for the funding support and China Postdoctoral Science Foundation for funding support (2021M690175), and thanks the financial support of the Frontier Crossover Project of Central Universities (2021CDJQY-029).

Institutional Review Board Statement: Not applicable.

Informed Consent Statement: Not applicable.

Data Availability Statement: Not applicable.

Conflicts of Interest: The authors declare no conflict of interest.

Sample Availability: Samples of the compounds are not available from the authors.

References

1. Song, Y.; Ji, Q.; Du, Y.-J.; Geng, J.-B. The dynamic dependence of fossil energy, investor sentiment and renewable energy stock markets. *Energy Econ.* **2019**, *84*, 104564. [[CrossRef](#)]
2. Moh, D.Y.; Zhang, H.; Wang, S.; Yin, X.; Qiao, R. Soaking in CO₂ huff-n-puff: A single-nanopore scale study. *Fuel* **2022**, *308*, 122026. [[CrossRef](#)]
3. Zhang, L.; Liu, C.; Li, Q. Molecular simulations of competitive adsorption behavior between CH₄-C₂H₆ in K-illite clay at supercritical conditions. *Fuel* **2020**, *260*, 116358. [[CrossRef](#)]
4. Gong, L.; Wang, J.; Gao, S.; Fu, X.; Liu, B.; Miao, F.; Zhou, X.; Meng, Q. Characterization, controlling factors and evolution of fracture effectiveness in shale oil reservoirs. *J. Pet. Sci. Eng.* **2021**, *203*, 108655. [[CrossRef](#)]
5. Belu Mănescu, C.; Nuño, G. Quantitative effects of the shale oil revolution. *Energy Policy* **2015**, *86*, 855–866. [[CrossRef](#)]
6. Zhang, Y.; Fang, T.; Ding, B.; Wang, W.; Yan, Y.; Li, Z.; Guo, W.; Zhang, J. Migration of oil/methane mixture in shale inorganic nano-pore throat: A molecular dynamics simulation study. *J. Pet. Sci. Eng.* **2020**, *187*, 106784. [[CrossRef](#)]
7. Taheri-Shakib, J.; Kantzas, A. A comprehensive review of microwave application on the oil shale: Prospects for shale oil production. *Fuel* **2021**, *305*, 121519. [[CrossRef](#)]

8. Kong, S.; Feng, G.; Liu, Y.; Li, K. Potential of dimethyl ether as an additive in CO₂ for shale oil recovery. *Fuel* **2021**, *296*, 120643. [[CrossRef](#)]
9. Moh, D.Y.; Zhang, H.; Sun, S.; Qiao, R. Molecular anatomy and macroscopic behavior of oil extraction from nanopores by CO₂ and CH₄. *Fuel* **2022**, *324*, 124662. [[CrossRef](#)]
10. Zhang, L.; Liu, C.; Liu, Y.; Li, Q.; Cheng, Q.; Cai, S. Transport Property of Methane and Ethane in K-illite Nanopores of Shale: Insights from Molecular Dynamic Simulations. *Energy Fuels* **2020**, *34*, 1710–1719. [[CrossRef](#)]
11. Elwegaa, K.; Emadi, H.; Soliman, M.; Gamadi, T.; Elsharafi, M. Improving oil recovery from shale oil reservoirs using cyclic cold carbon dioxide injection—An experimental study. *Fuel* **2019**, *254*, 115586. [[CrossRef](#)]
12. Fakher, S.; Imqam, A. Application of carbon dioxide injection in shale oil reservoirs for increasing oil recovery and carbon dioxide storage. *Fuel* **2020**, *265*, 116944. [[CrossRef](#)]
13. Jia, B.; Tsau, J.-S.; Barati, R. A review of the current progress of CO₂ injection EOR and carbon storage in shale oil reservoirs. *Fuel* **2019**, *236*, 404–427. [[CrossRef](#)]
14. Middleton, R.S.; Carey, J.W.; Currier, R.P.; Hyman, J.D.; Kang, Q.; Karra, S.; Jiménez-Martínez, J.; Porter, M.L.; Viswanathan, H.S. Shale gas and non-aqueous fracturing fluids: Opportunities and challenges for supercritical CO₂. *Appl. Energy* **2015**, *147*, 500–509. [[CrossRef](#)]
15. Lashgari, H.R.; Sun, A.; Zhang, T.; Pope, G.A.; Lake, L.W. Evaluation of carbon dioxide storage and miscible gas EOR in shale oil reservoirs. *Fuel* **2019**, *241*, 1223–1235. [[CrossRef](#)]
16. Lu, Y.; Chen, X.; Tang, J.; Li, H.; Zhou, L.; Han, S.; Ge, Z.; Xia, B.; Shen, H.; Zhang, J. Relationship between pore structure and mechanical properties of shale on supercritical carbon dioxide saturation. *Energy* **2019**, *172*, 270–285. [[CrossRef](#)]
17. Wang, S.; Javadpour, F.; Feng, Q. Fast mass transport of oil and supercritical carbon dioxide through organic nanopores in shale. *Fuel* **2016**, *181*, 741–758. [[CrossRef](#)]
18. Zhang, W.; Feng, Q.; Wang, S.; Xing, X. Oil diffusion in shale nanopores: Insight of molecular dynamics simulation. *J. Mol. Liq.* **2019**, *290*, 111183. [[CrossRef](#)]
19. Zhong, J.; Wang, P.; Zhang, Y.; Yan, Y.; Hu, S.; Zhang, J. Adsorption mechanism of oil components on water-wet mineral surface: A molecular dynamics simulation study. *Energy* **2013**, *59*, 295–300. [[CrossRef](#)]
20. Chen, L.; Zhang, L.; Kang, Q.; Viswanathan, H.S.; Yao, J.; Tao, W. Nanoscale simulation of shale transport properties using the lattice Boltzmann method: Permeability and diffusivity. *Sci. Rep.* **2015**, *5*, 8089. [[CrossRef](#)]
21. Wang, S.; Feng, Q.; Javadpour, F.; Yang, Y.-B. Breakdown of Fast Mass Transport of Methane through Calcite Nanopores. *J. Phys. Chem. C* **2016**, *120*, 14260–14269. [[CrossRef](#)]
22. Shuai, Z.; Xiaoshu, L.; Qiang, L.; Youhong, S. Thermal-fluid coupling analysis of oil shale pyrolysis and displacement by heat-carrying supercritical carbon dioxide. *Chem. Eng. J.* **2020**, *394*, 125037. [[CrossRef](#)]
23. De Lara, L.S.; Michelon, M.F.; Miranda, C.R. Molecular Dynamics Studies of Fluid/Oil Interfaces for Improved Oil Recovery Processes. *J. Phys. Chem. B* **2012**, *116*, 14667–14676. [[CrossRef](#)]
24. Nguyen, P.; Carey, J.W.; Viswanathan, H.S.; Porter, M. Effectiveness of supercritical-CO₂ and N₂ huff-and-puff methods of enhanced oil recovery in shale fracture networks using microfluidic experiments. *Appl. Energy* **2018**, *230*, 160–174. [[CrossRef](#)]
25. Seyyedi, M.; Mahzari, P.; Sohrabi, M. An integrated study of the dominant mechanism leading to improved oil recovery by carbonated water injection. *J. Ind. Eng. Chem.* **2017**, *45*, 22–32. [[CrossRef](#)]
26. Liu, L.; Bhatia, S.K. Molecular Simulation of CO₂ Adsorption in the Presence of Water in Single-Walled Carbon Nanotubes. *J. Phys. Chem. C* **2013**, *117*, 13479–13491. [[CrossRef](#)]
27. Song, J.; Liu, L.; Liu, C.; Gao, X. Interfacial resistance of gas transport through rigid and flexible zeolites. *Sep. Purif. Technol.* **2021**, *278*, 119529. [[CrossRef](#)]
28. Liu, X.; Zhang, D. A review of phase behavior simulation of hydrocarbons in confined space: Implications for shale oil and shale gas. *J. Nat. Gas Sci. Eng.* **2019**, *68*, 102901. [[CrossRef](#)]
29. Jorgensen, W.L.; Maxwell, D.S.; Tirado-Rives, J. Development and Testing of the OPLS All-Atom Force Field on Conformational Energetics and Properties of Organic Liquids. *J. Am. Chem. Soc.* **1996**, *118*, 11225–11236. [[CrossRef](#)]
30. Harris, J.G.; Yung, K.H. Carbon Dioxide's Liquid-Vapor Coexistence Curve and Critical Properties as Predicted by a Simple Molecular Model. *J. Phys. Chem.* **1995**, *99*, 12021–12024. [[CrossRef](#)]
31. Cygan, R.T.; Liang, J.-J.; Kalinichev, A.G. Molecular Models of Hydroxide, Oxyhydroxide, and Clay Phases and the Development of a General Force Field. *J. Phys. Chem. B* **2004**, *108*, 1255–1266. [[CrossRef](#)]
32. Liu, B.; Wang, C.; Zhang, J.; Xiao, S.; Zhang, Z.; Shen, Y.; Sun, B.; He, J. Displacement Mechanism of Oil in Shale Inorganic Nanopores by Supercritical Carbon Dioxide from Molecular Dynamics Simulations. *Energy Fuels* **2016**, *31*, 738–746. [[CrossRef](#)]
33. Delhommelle, J.; Millié, P. Inadequacy of the Lorentz-Berthelot combining rules for accurate predictions of equilibrium properties by molecular simulation. *Mol. Phys.* **2001**, *99*, 619–625. [[CrossRef](#)]
34. Plimpton, S. Fast Parallel Algorithms for Short-Range Molecular Dynamics. *J. Comput. Phys.* **1995**, *117*, 1–19. [[CrossRef](#)]
35. Purton, J.A.; Crabtree, J.C.; Parker, S.C. DL_MONTE: A general purpose program for parallel Monte Carlo simulation. *Mol. Simul.* **2013**, *39*, 1240–1252. [[CrossRef](#)]

36. Moulton, O.A.; Tsimpanogiannis, I.N.; Panagiotopoulos, A.Z.; Economou, I.G. Self-diffusion coefficients of the binary (H₂O + CO₂) mixture at high temperatures and pressures. *J. Chem. Thermodyn.* **2016**, *93*, 424–429. [[CrossRef](#)]
37. Zhao, X.; Jin, H. Correlation for self-diffusion coefficients of H₂, CH₄, CO, O₂ and CO₂ in supercritical water from molecular dynamics simulation. *Appl. Therm. Eng.* **2020**, *171*, 114941. [[CrossRef](#)]